SCIENTIFIC REPORTS

OPEN

SUBJECT AREAS:
PHOTOCATALYSIS
POROUS MATERIALS
MATERIALS CHEMISTRY
RENEWABLE ENERGY

Received
4 March 2013

Accepted
28 March 2013

Published
16 April 2013

Correspondence and requests for materials should be addressed to J.Y. (Jinhua.YE@nims.go.jp)

Leaf-architectured 3D Hierarchical Artificial Photosynthetic System of Perovskite Titanates Towards CO_2 Photoreduction Into Hydrocarbon Fuels

Han Zhou[1,5], Jianjun Guo[1,3], Peng Li[1,3], Tongxiang Fan[5], Di Zhang[5] & Jinhua Ye[1,2,3,4]

[1]International Center for Materials Nanoarchitectonics (WPI-MANA), National Institute for Materials Science (NIMS), 1-1, Namiki, Tsukuba, Ibaraki 305-0044, Japan, [2]Environmental Remediation Materials Unit, National Institute for Materials Science (NIMS), 1-1 Namiki, Tsukuba, Ibaraki, 305-0044, Japan, [3]Graduate School of Chemical Sciences and Engineering, Hokkaido University, Sapporo, Japan, [4]TU–NIMS Joint Research Center, School of Materials Science and Engineering, Tianjin University, 92 Weijin Road, Nankai District, Tianjin 300072, P. R. China, [5]State Key Lab of Metal Matrix Composites, Shanghai Jiaotong University, Shanghai, 200240, P. R. China.

The development of an "artificial photosynthetic system" (APS) having both the analogous important structural elements and reaction features of photosynthesis to achieve solar-driven water splitting and CO_2 reduction is highly challenging. Here, we demonstrate a design strategy for a promising 3D APS architecture as an efficient mass flow/light harvesting network relying on the morphological replacement of a concept prototype-leaf's 3D architecture into perovskite titanates for CO_2 photoreduction into hydrocarbon fuels (CO and CH_4). The process uses artificial sunlight as the energy source, water as an electron donor and CO_2 as the carbon source, mimicking what real leaves do. To our knowledge this is the first example utilizing biological systems as "architecture-directing agents" for APS towards CO_2 photoreduction, which hints at a more general principle for APS architectures with a great variety of optimized biological geometries. This research would have great significance for the potential realization of global carbon neutral cycle.

Facing increasing demands for energy and environmental concerns, the development of an "artificial photosynthetic system" (APS) in conceptually simpler form to achieve results of natural photosynthesis that is coupling solar-driven water splitting and CO_2 reduction in a way that eliminates the need for an external, sacrificial electron donor is one of the great challenges for the use of renewable energy and a sustainable development[1–5]. Practically, "CO_2 reduction" is more urgent than "water splitting" because it not only contributes to global carbon cycling for carbon neutral organic fuels, mimicking what real leaves do (natural carbon fixation), but also alleviating global climate changes[6,7]. However, as CO_2 is a relatively inert and stable compound, its reduction is quite challenging. The photoreduction of CO_2 has been widely studied for a long time as well as water splitting[8–11]. For heterogeneous photocatalysts, many efforts still focus on TiO_2-based[10,12,13] materials while other catalysts such as Zn_2GeO_4[14–16], $ZnGa_2O_4$[17], $CaFe_2O_4$[18], $ALa_4Ti_4O_{15}$ (A = Ca, Sr, and Ba)[19], WO_3[20] and so forth have also been reported in recent years. However, the progress achieved in this field had not been as dramatic as that in water splitting for a few decades because of the low efficiencies, limited photocatalysts and/or requiring the use of sacrificial reducing agents. Generally, for the gas-phase reaction, multifold factors are involved including gas capture (gas diffusion/adsorption), light harvesting and gas conversion (multi-electron chemical reactions). We[15–17] and others[14] have recently demonstrated that mesoporous structured photocatalysts can significantly enhance the gas-phase reaction efficiency. However, gas diffusion limitation has still been a concerning problem for micro/mesoporous systems[21]. Thus, it is highly challenging but desirable to develop a promising and ideal APS having both the analogous important structural elements and reaction features of natural photosynthesis by constructing (i) efficient mass flow network with 3D multiple-scaled hierarchical porosity to suffer minimum gas diffusion, and high surface areas for improved overall reaction performances[22,23]. (ii) unique 3D architecture for enhanced light harvesting. (iii) suitable catalysts with sufficiently negative conduction band for strong reduction potential.

One promising approach to circumvent such issues concerns biomimetics[24]. Nature, over billions of years, has achieved in the leaf a great technological feature. A natural leaf is a synergy of complex architectures and functional components to produce an amazing bio-machinery for photosynthesis, that is efficiently harvest solar energy and convert water and carbon dioxide into carbohydrates and oxygen[25]. Natural leaves have demonstrated the perfect assembly of hierarchical levels of porosity into 3D elaborated architectures with high porosity, high connectivity and high surface areas for efficient mass flow including gas exchange[26] for photosynthesis and water transportation[27] for photosynthesis as well as for transpiration. Furthermore, the intrinsic 3D architecture within natural leaves strongly favors light harvesting[28,29] *via* a synergy of multifold effects including the focusing of light by the lens-like epidermal cells, the multiple scattering and absorbance of light within the veins' porous network, the light propagation in the elongated columnar cells in palisade parenchyma acting as light guides, the enhanced effective light pathlength and light scattering by the irregular-shaped, loosely-packed spongy mesophyll cells and so forth.

Inspired by this, in the present work, leaf's 3D unique hierarchical architecture would be selected as an ideal parent model (template) to emphasize the potential of our strategy in terms of the construction of an APS. We present a promising APS of perovskite titanates ($ATiO_3$, A = Sr, Ca, and Pb) by preserving very fine morphological details of leaves' architectures for CO_2 photoreduction into hydrocarbon fuels. The process uses artificial sunlight as the energy source, water as an electron donor and CO_2 as the carbon source to create hydrocarbon fuels (mainly carbon monoxide and methane), mimicking what real leaves do. Various cocatalysts (Au, Ag, Cu, Pt, RuO_2, and NiO_x) are loaded for enhanced activity, among which Au as a suitable cocatalyst, exhibits the best performance. The study demonstrates that leaves' unique 3D hierarchical architectures, as a concept prototype would pave a new pathway for the development of an efficient mass flow network for improved gas diffusion as well as enhanced light harvesting. To the best of our knowledge this is the first example utilizing biological systems as an "architecture-directing agent" for the construction of APS for CO_2 photoreduction. This research would have great significance for the potential realization of global carbon neutral cycle.

Results

Morphology and Key processes in NPS. It is useful to start with a review of some of the key elements and processes of natural photosynthesis that are to be reproduced functionally. Fig. 1 shows schematically the key processes that we shall be concerned with. Typically, natural photosynthesis is the process by green leaves use sunlight as the energy source, CO_2 of the atmosphere, and water as chemicals to carry out two important reactions required for survival and growth of humanity: decomposition of water to molecular

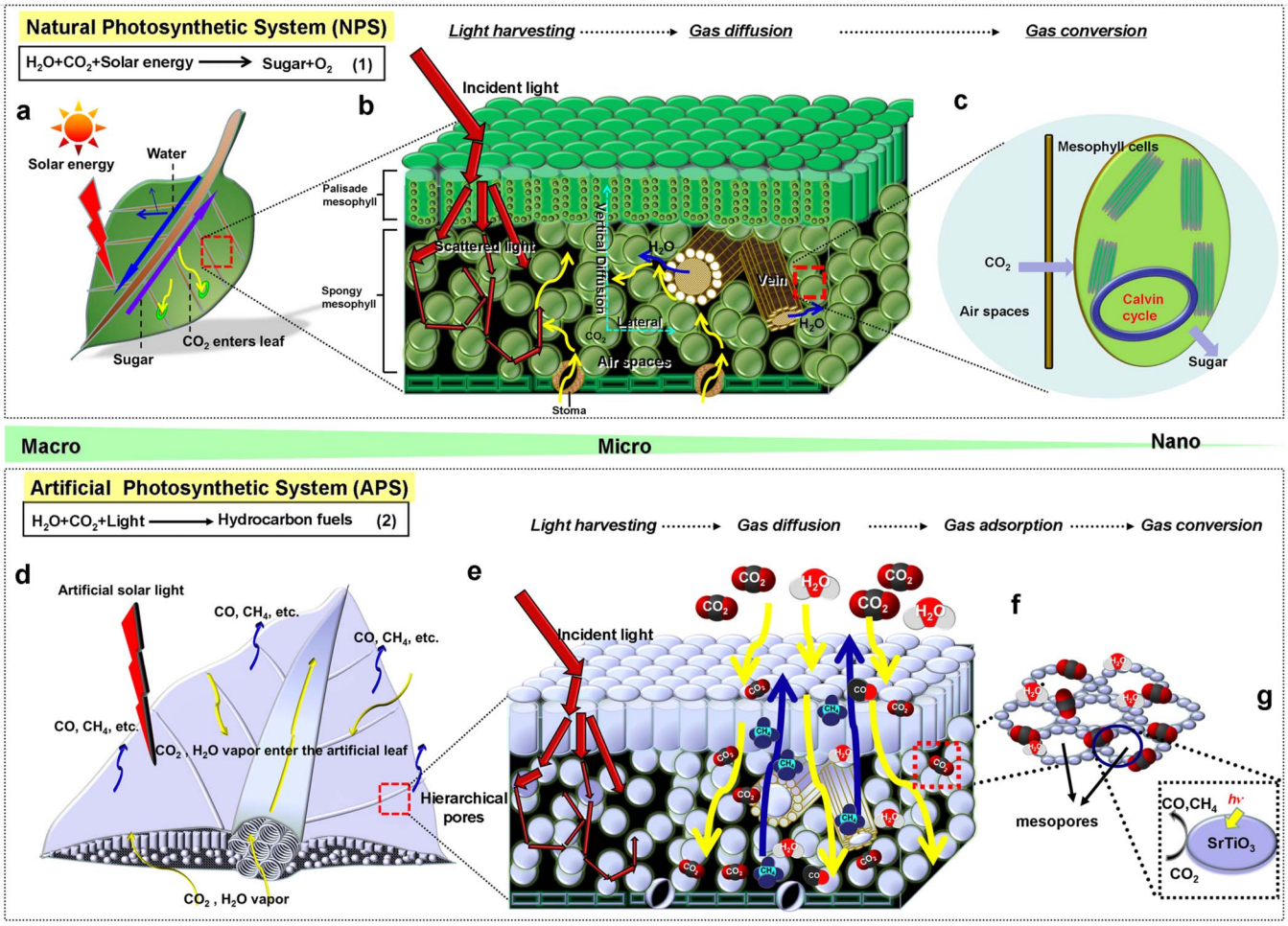

Figure 1 | Schematic illustration and comparison of the key processes in natural photosynthetic system (NPS) and artificial photosynthetic system (APS). (a) Basic process of photosynthesis in NPS at macroscale. (b) Light harvesting and gas diffusion processes in NPS at microscale. (c) Gas conversion process in mesophyll cells at nanoscale. (d) Basic process of artificial photosynthesis in APS at macroscale. (e) Light harvesting and gas diffusion processes in APS at microscale. (f) Gas adsorption process in APS at nanoscale. (g) Gas conversion process in APS at nanoscale.

oxygen, accompanied by reduction of CO_2 to carbohydrates and other carbon-rich products[25] (Fig. 1a, Equation 1).

Leaves' 3D architectures at multi-scaled levels are designed as a promising prototype for efficient mass flow including gas exchange, water transportation (Fig. 1b and Fig. 2) and light harvesting (Fig. 1b). Leaves generally have a thin shape with large surface areas which means a short distance for CO_2 to diffuse in and O_2 to diffuse out easily. Gases (*e.g.* CO_2) enter the leaf through stomata - usually in the lower surface of the leaf (Fig. 1b and Fig. 2e)[26]. Once inside the leaf, CO_2 can diffuse along its concentration gradients through the air spaces, which are in direct contact with the spongy and palisade mesophyll cells (Fig. 1b and Fig. 2f). The main gas exchange surfaces in plants are the irregular-shaped, loosely-packed spongy mesophyll cells[26] with numerous large interconnecting air spaces (Fig. 2e) in the range of micrometers which are much larger than the mean free path of gas molecules, thus gases suffer a minimum intercellular diffusion within such interconnected networks (Fig. 1b). Despite the appearance of close packing (Fig. 1b and Fig. 2f), palisade cell surfaces are generally exposed to intercellular airspace. Inward diffusion of CO_2 to chloroplasts is thereby facilitated. Intercellular diffusion is fundamentally a 3D process occurring with negligible resistance, because of molecular diffusion[26]. Lateral diffusion in leaves is thus likely to occur preferentially in the spongy parenchyma whereas vertical diffusion encompasses both spongy and palisade tissue (Fig. 1b). CO_2 then diffuse throughout the mesophyll cells, dissolve in wet cell walls, where it may dissociate into bicarbonate or remain as CO_2[30]. In one or the other form, it diffuses in the liquid phase through the cell wall and into a chloroplast where it enters the Calvin cycle and completes its journey as a photosynthetic product (Fig. 1c)[30].

Another dominating structure of leaves are the leaf veins, which form a venation system in leaf lamina for efficient hydraulic supply, delivery of nutrients and sugars to each part of a leaf, and biomechanical support[31]. Macroscopically, the 2D optical images of a natural leaf (Fig. 2b and 2c) indicate the inter-connected branching venation networks on multi-length scales. After the petiole, water moves through the xylem conduits within veins arranged in a reticulate hierarchy, with vein conductivity decreasing and vein density increasing from low- to higher-order veins (Fig. 2c). Water exits the xylem and moves through bundle sheath, mesophyll, bundle sheath extensions, and/or epidermis and then evaporates and diffuses from the stomata[32]. The leaf hydraulic system can be analyzed as a hierarchical inter-connected pipe network (Fig. 2d, 2g, 2i and 2j). Microscopically, Veins are composed of hierarchical cylindrical tubes at the length of several to tens of micrometers (Fig. 2g and 2j). Each tube is stacked by stacked layers of interconnected hollow sub-microtubes (Fig. 2h). Furthermore, the unique architecture of various structural elements and their organization way within the leaf play a significant role for the promotion of light harvesting efficiency (Supplementary Fig. S1)[28].

Based on this, faithfully preservation of leaf's architectures is expected to realize a promising APS with enhanced mass flow and light harvesting ability. Biotemplated materials have been developed in the last decade[33–36], However, most of which are restricted to binary compounds (*e.g.* single metal oxides) while biologically synthesis of multi-metallic oxides (*e.g.* ternary or quarternary compounds) with hierarchical porous structures has rarely reported and is highly challenging as it requires multiple precursors with strong interactions between each other in liquid phase as well as matching reaction/infiltration rates. Furthermore, biotemplated materials for CO_2 photoreduction have not been reported so far. It is noteworthy that many kinds of multi-metallic oxides have shown high activities in water splitting as well as in many other energy conversion areas[37–40]. Perovskite, ABO_3 type materials (*e.g.* $SrTiO_3$, $CaTiO_3$) are considered as promising photocatalysts for water splitting, because of their high reduction and oxidation potential[38]. $SrTiO_3$ has been known as a photocatalyst capable of decomposing H_2O into H_2 and O_2 without applying an external bias potential[41]. Cubic perovskite $CaTiO_3$ displays a suitable conduction/valence band positions (as desirable for photocatalytic water splitting). $PbTiO_3$ is a visible light responsive photocatalyst. Therefore, these photocatalysts are expected to be active for CO_2 reduction. So in this research, perovskite titanates $ATiO_3$ (A = Sr, Ca, Pb) are first chosen as the target photocatalysts for the construction and demonstration of a promising APS architecture.

Synthesis and characterization of APS. Here, a modified sol-gel method is used for the synthesis of leaf-architectured APS of $ATiO_3$ (See Methods). After calcination at 600°C, organics could be removed completely according to TGA data (Supplementary Fig. S2) leaving crystalline perovskite titanates as demonstrated by XRD (Fig. 3a). The obtained APS exhibits morphological features of NPS at multilevel scales (Fig. 2). Macroscopically, the APS has a thin shape with shrinkage of about 50% of the original dimensions after calcination (Fig. 2k). The inter-connected branching venation networks are still clearly visible in APS (Fig. 2l). At the micro scale, the APS inherit the 3D architecture features, typically including the epidermal surfaces with numerous micrometer-sized stoma (Fig. 2n), the irregular-shaped, loosely-packed spongy mesophyll cells with numerous large interconnecting air spaces (Fig. 2o) and the hierarchical porous network of veins (Fig. 2p and 2q). Such APS is constructed by a 3D hierarchical macropore network of various shapes, dimensions and orientations which endow it with a relatively robust feature (Fig. 2m). In the meanwhile, the macropore framework is composed of mesoporous crystalline ATO building blocks (Fig. 2r, 2s and Supplementary Fig. S3). The pore diameter is estimated to be ~7 nm for STO (Fig. 2s), which coincides with BET nitrogen adsorption-desorption data (Supplementary Table S1). The porous properties of the products were assessed by N_2 gas adsorption (Supplementary Table S1) for mesoporosity and mercury porosimetry (Fig. 3b and Supplementary Fig. S4) for meso/macroporosity, respectively.

CO_2 photoreduction activity. Artificial photosynthesis is carried out on ATO series using H_2O and CO_2 as the reactants under UV-Vis light irradiation. Bare $SrTiO_3$ (Fig. 4a) and $CaTiO_3$ (Supplementary Fig. S5) evolve CO and CH_4 as the main products for CO_2 reduction in the absence of any sacrificial agents. The evolution amount of CO is larger than that of CH_4 both for bare STO and CTO series. It is well known that the CO_2 photoreduction mainly undergoes two courses, including oxidation and reduction processes. In the oxidation process, H_2O is oxidized to O_2 ($2H_2O + 4h^+ \rightarrow O_2 + 4H^+$). In the reduction course, there is a chain reaction to reduce CO_2 to CH_4 ($CO_2 + 2H^+ + 2e^- \rightarrow CO + H_2O$, $CO_2 + 4H^+ + 4e^- \rightarrow HCHO + H_2O$, $CO_2 + 6H^+ + 6e^- \rightarrow CH_3OH + H_2O$, $CO_2 + 8H^+ + 8e^- \rightarrow CH_4 + 2H_2O$)[9], as shown in Supplementary Table S2. The position of the conduction band and valence band of the $SrTiO_3$ and $CaTiO_3$ could be calculated empirically according to eq 1:

$$E_{CB} = X - E_C - 0.5E_g \quad (1)$$

where E_c is the energy of free electrons on the hydrogen scale (4.5 eV), X is the electronegativity of the semiconductor, and E_g is the band-gap energy of the semiconductor according to UV-Vis spectrum (Supplementary Fig. S6). The edges of the valence band (E_{VB}) of STO and CTO were determined to be 2.32 V and 2.64 V (vs normal hydrogen electrode, NHE) respectively, more positive than that of $E^\circ(H_2O/H^+)$ ($H_2O \rightarrow 1/2O_2 + 2H^+ + 2e^-$, E° redox = 0.82 V vs NHE), and the edges of the conduction band were estimated to be −0.88 V and −0.86 V (vs NHE) respectively, more negative than that of E° (CO_2/CO) ($CO_2 + 2e^- + 2H^+ \rightarrow CO + H_2O$, E° redox = −0.53 V vs NHE) and E° (CO_2/CH_4) ($CO_2 + 8e^- + 8H^+ \rightarrow CH_4 + 2H_2O$, E° redox = −0.24 V vs NHE). This indicates that the photogenerated electrons and holes on the

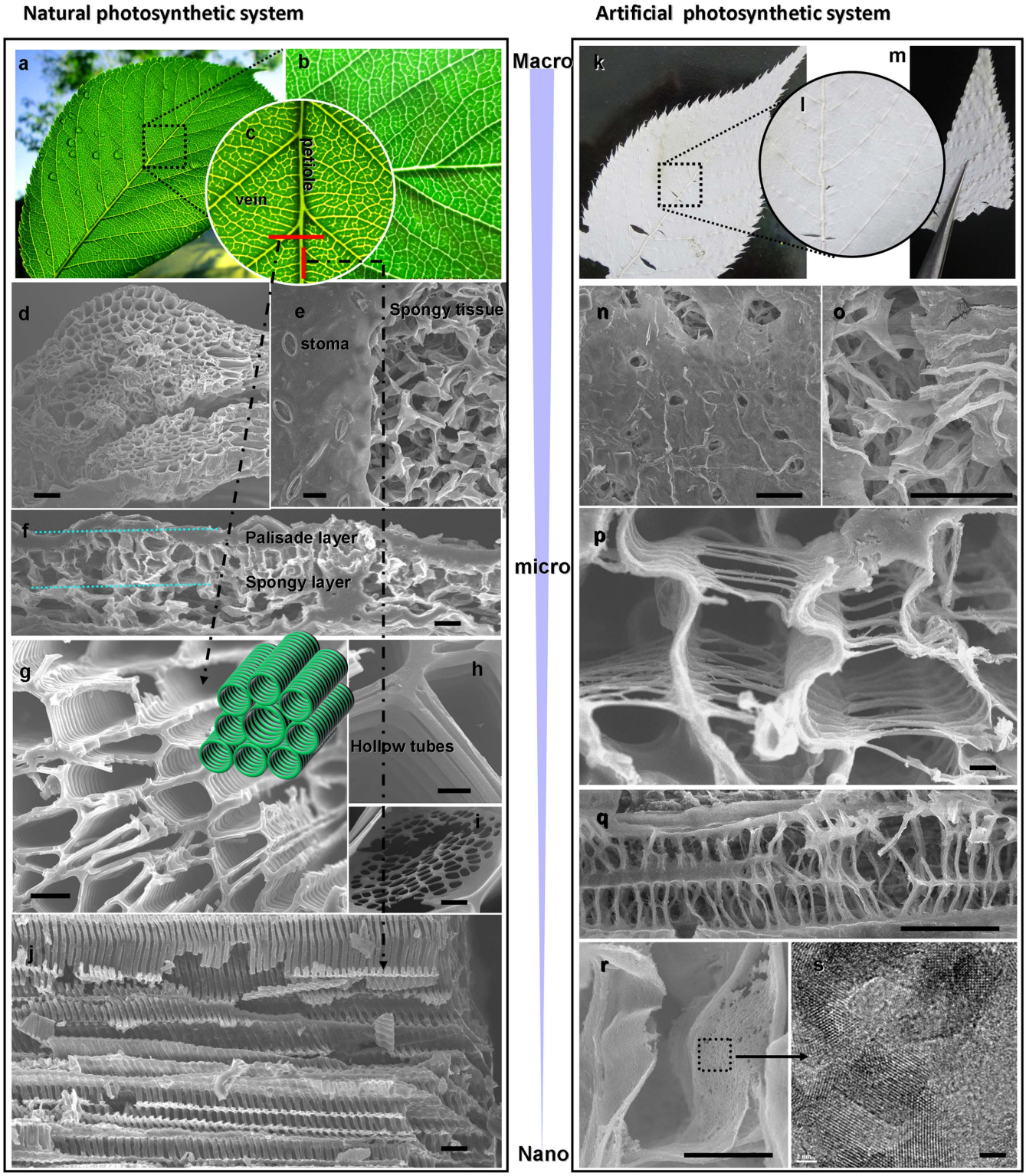

Figure 2 | Morphology comparison between NPS and APS (leaf-architectured $SrTiO_3$) from macro-, micro- to nanoscales. (a) Optical image of *Cherry Blossom* leaf. (b, c) Magnified optical images of the branching network of veins. FESEM images of (d) the cross-section of the vein porous architecture. (e) the lower epidermis. (f) the cross-section, indicating the differentiation of leaf mesophyll into palisade and spongy layers. (g) magnified image of the cross section of venation architecture, with the inset of the 3D illustration. (h) the stacked interconnected hollow sub-microtubes of the veins. (i) sub-micrometer sized pores on the walls. (j) the cross section of venation architecture axially. (k) Optical image of the APS. (l) magnified image of (k), indicating the branching network of artificial veins in APS. (m) a piece of APS hold by tweezer, indicating the relatively robust feature. FESEM images of (n) the surfaces of APS. (o) Magnified image of the surfaces, indicating the morphologies derived from the spongy tissues. (p) the cross section of venation architecture in APS. (q) the cross section of venation architecture axially in APS. (r) Magnified image of the walls. (s) TEM image of the mesoporous structures of $SrTiO_3$. (d) scale bar, 20 μm. (e, f, g, j, n, o, q) scale bar, 10 μm. (h, i, p, r) scale bar, 1 μm. (s) scale bar, 2nm. For NPS, the samples were carbonized before SEM observation.

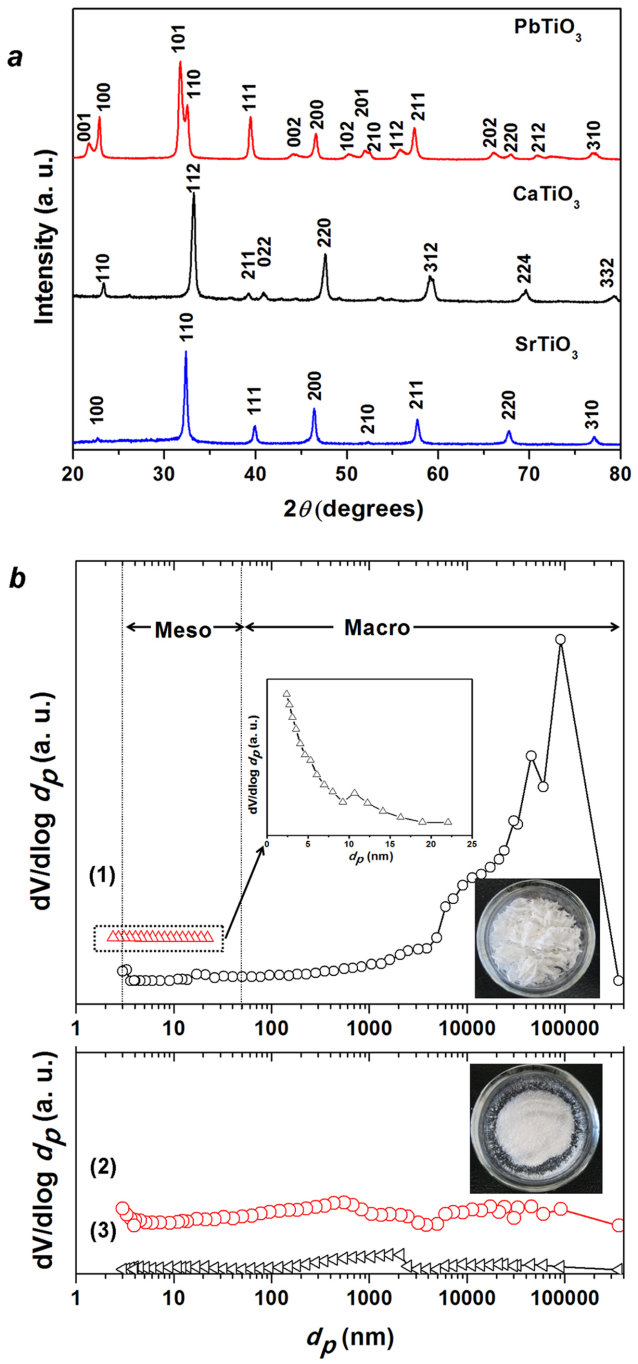

Figure 3 | (a) XRD patterns of $ATiO_3$ (A = Sr, Ca, Pb) series. (b) Comparative hierarchical pore size distributions of $SrTiO_3$ series derived from the N_2 (BJH model, red triangles) adsorption (the inset of (1)), and mercury intrusion porosimetry, respectively. The plots are offset for clarity. (1) leaf-architectured APS_{STO}, with the inset of sample's optical image. (2) the corresponding powder constituents of APS_{STO}, with the inset of sample's optical image. (3) referenced STO synthesized without templates.

irradiated STO and CTO can react with adsorbed CO_2 and H_2O to produce CO and CH_4. Other products such as formate, formaldehyde, and methanol (HCOOH, HCHO, CH_3OH) were not detected, probably because of the strong oxidation power of photogenerated valence band holes (or OH radicals) that can react with intermediates and products of CO_2 conversion in reactions[42,43], making the net hydrocarbon yield negligible.

Notably, leaf-architectured APS of STO and CTO exhibit about a 1.5~2.2 fold and 3.5~4 fold improvement in activities than the corresponding powder constituents of APS and referenced STO/or CTO synthesized without templates (Fig. 4a and Supplementary Fig. S5). This is related to multiple processes mainly including gas diffusion and light harvesting. As shown in Figure 1d, CO_2 and H_2O vapor enter the APS through the hierarchical macro/mesopores (*e.g.* epidermal, veins, stoma, etc.) channels. Different from the NPS with only stoma as the gas entrance gate, APS is much more permeable for gas molecules due to its highly hierarchical porous feature. Then the entered gas molecules diffuse through the pore network, collide with the pore walls, adsorbed and react on active sites on these walls. As characterized above, the APS is comprised of a 3D hierarchical network of interconnected pores of varying shapes, diameters, and orientations. When the diameter of the pore is much greater than the mean free path of the gas molecules, the diffusing molecules will interact with each other more than with the pore walls, thereby minimizing the wall effects on the transport[44]. In this case, the pore diffusivity is essentially the same as the molecular diffusivity, in which the diffusion coefficient is much larger than that in mesopores. Take CO_2 as an instance, the diffusion coefficient (D) in mesopores of APS_{STO} is calculated to be about 0.0189 cm^2/s while that in macropore network of APS_{STO} is about ~0.097 cm^2/s which is about 5–6 fold. By contrast, though there are still a few macropores in the corresponding powder constituents of APS_{STO} *via* grounding as demonstrated by SEM (Supplementary Fig. S7a), TEM (Supplementary Fig. S7b and S7c), and mercury porosimeter (Fig. 3b), the quantity of macropores decreases dramatically while the size distribution of macropores is also entirely different (Fig. 3b). Thus, the gas diffusion rate is smaller and longer time is required for reactants (CO_2 and H_2O vapor) to move into the deeper as well as for products (e.g. CO, CH_4, etc.) to move from the deeper layer into the atmosphere. Detailed explanation and calculations of gas diffusion are discussed in the Supplementary Discussion. Besides, we think that leaf's high connectivity of hierarchical pores and the branching network of venation may promote the gas diffusion. Modeling and computation is worth further study. On the other hand, as the 3D hierarchical architecture of NPS strongly favors light harvesting as discussed in Figure S1, the APS architecture would be favorable for capture more light and transfer light into the deeper layer of the 3D system, thus enhance light harvesting. Therefore, the difference in CO_2 reduction activity observed between APS_{STO} and powdered APS_{STO} constituents can be explained by the distinct 3D hierarchical architecture. For referenced STO/or CTO, since the particles are closely packed which not only restricts efficient gas diffusion but also light harvesting as compared in Supplementary Fig. S9, so the activities are lower. Furthermore, the higher surface area and higher volume of mesopores (Supplementary Table S1) of the APS provide more reaction sites, thus enhancing the overall performances. So the improvement of the activities in APS is the synergy of the efficient mass flow 3D architecture for high gas diffusion coefficient and hence high gas diffusion rates of the reactants and the products, the complex morphology for enhanced light harvesting and the more reaction sites arising from the mesoporous structures and high specific surface areas.

To overcome the thermochemically unfavorable one-electron reduction of CO_2, the proton-coupled multielectron transfer (PCET) (Supplementary Table S2) should be facilitated by modifying the surface properties of photocatalysts (*e.g.,* loading a co-catalyst that serves as an electron reservoir)[45,46]. A series of cocatalysts were loaded onto STO samples for comparison (Fig. 4b and Supplementary Table S5). Loading Pt cocatalyst on STO could enhance the photocatalytic activity for water splitting[47], but surprisingly not CO_2 reduction in STO, probably because although Pt functions as an efficient cocatalyst for H_2 evolution, it also catalyzes the reverse reaction of water formation from H_2 and O_2. Furthermore, loading

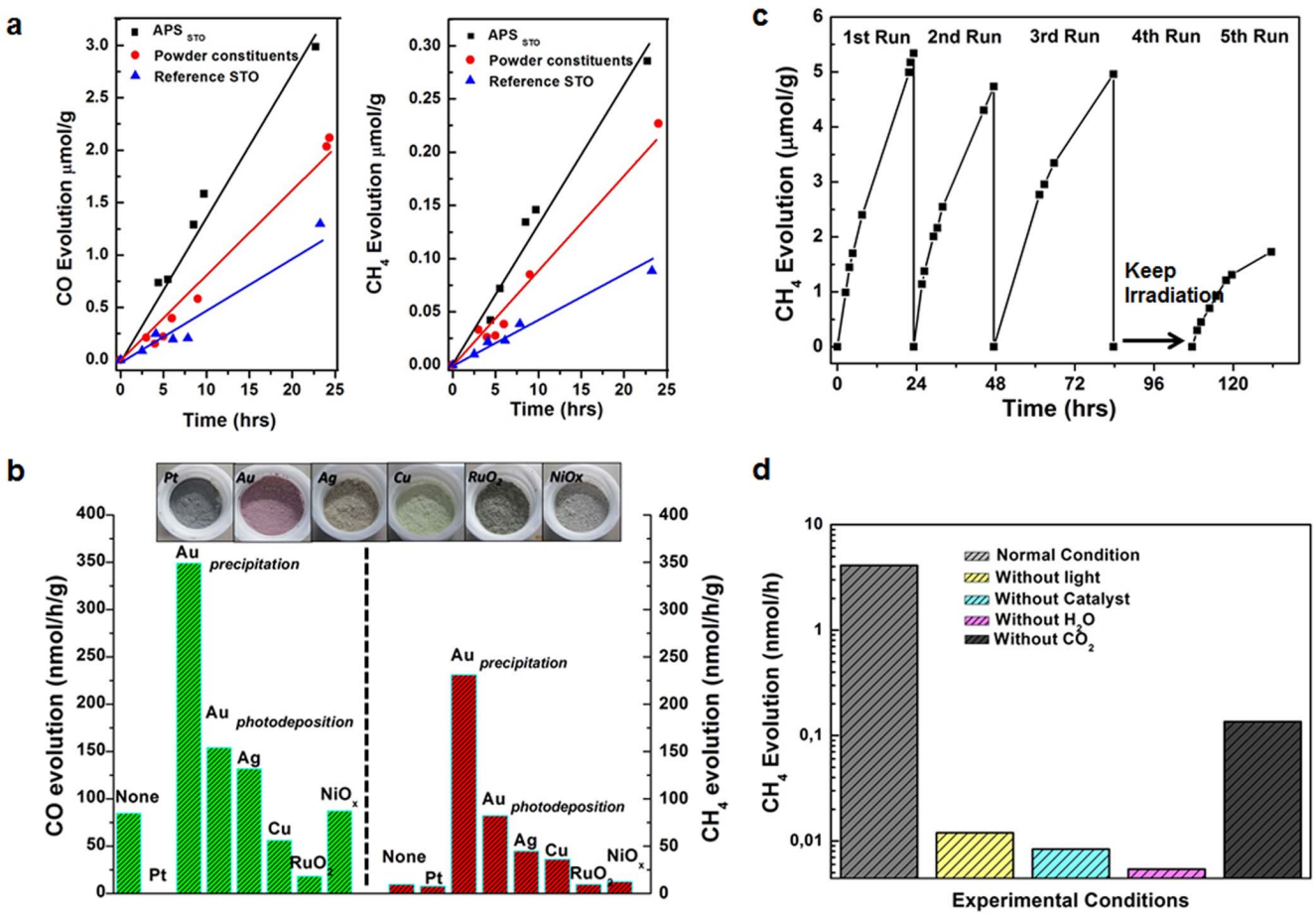

Figure 4 | Photocatalytic CO_2 reduction activities. (a) CO and CH_4 evolution on bare $SrTiO_3$ series. (b) CO and CH_4 evolution on APS_{STO} loaded with different cocatalysts. (c) Photocatalytic formation of CH_4 on Au (1 wt%)-APS_{STO} synthesized under CO_2 with prolonged irradiation (up to 130 hrs). Au cocatalyst was synthesized *via* a precipication method. The reaction sample was degassed after each run (~24 h), CO_2 (80 kPa) was introduced to it, and then the vessel was irradiated again. (d) CH_4 evolution in reference experiments in the conditions without H_2O, CO_2, light irradiation, and catalyst compared with that in normal conditions. $Au_{photodeposition}$ (1 wt%)-APS_{STO} was measured as the normal condition.

with Pt could significantly promote the so-called process of PSRM (Photocatalytic Steam Reforming of Methane)[48]. When Au, Ag and Cu cocatalysts (Supplementary Fig. S10 and S11) were loaded respectively, photocatalytic activities for CO_2 reduction into CO increased for Au and Ag. It has been reported that Au, Ag are highly active electrocatalysts for electrochemical reduction of CO_2 to form CO selectively in an aqueous $KHCO_3$ solution[49,50]. This fact indicated that the Au or Ag cocatalyst functioned as a CO_2 reduction site to form CO. In the meanwhile, the CH_4 evolution activity increased significantly, with the order of Au > Ag > Cu (Fig. 4b). Loading methods of cocatalysts would have significant effects on the photoreduction activity[19]. Take Au as an instance, a precipitation method is better than a photodeposition method, with the CH_4 evolution activity up to almost three-fold increase (Fig. 4b and Supplementary Table S5). The difference in the activity was due to the differences in the size and homogeneity of loaded Au cocatalysts[19]. The size of Au is in the range of 5–7 nm (Supplementary Fig. S11b) by a photodeposition method while the average size is only about 2 nm *via* a precipitation method[51]. For all samples, there is no oxygen detected. The oxygen generated by the water oxidation is partially used for the oxidation of the evolved products (HCOOH, HCHO, CO, etc.)[46,47] and partially is consumed by surface oxygen defects of the photocatalysts[52]. For Au, Ag, Cu, NiO_x systems, besides CO and CH_4, other hydrocarbon compounds (C_2H_4 and C_2H_6) were also generated in the reaction. However, the productions of these organic compounds were much lower than that of CH_4. These results suggest that the long chain organic molecules are generated *via* photocatalytic reforming of CH_4, and CH_4 is the source of this reaction[53]. The Au cocatalyst was also effective for CO_2 reduction over $CaTiO_3$ and $PbTiO_3$ photocatalysts (Supplementary Fig. S12). PTO alone evolved negligible CH_4 under UV and visible light irradiation, due to its relatively weak reduction power and strong oxidation potential. Loading with 1wt% Au increases its activities for CH_4 evolution, still much lower than that of STO and CTO series (Supplementary Fig. S12).

We checked the durability of $Au_{precipitation}$-APS_{STO} as a photocatalyst. Fig. 4c shows CH_4 formation by $Au_{precipitation}$ (1 wt%)-APS_{STO} during prolonged irradiation, up to 130 hrs. After each run (~24 h irradiation), the reaction vessel was degassed and CO_2 (80 kPa) was introduced to it again. As shown in Fig. 4c, the photocatalyst still maintained most of its intrinsic photocatalytic activity after three~four runs (up to 80 hrs). However, the photocatalytic activity was not restored to its former state during the 5th run. This indicates that deactivation of Au (1 wt%)-APS_{STO} as a photocatalyst proceeded during the long irradiation, which might because the metal surfaces become poisoned and deactivated by the reduction products[54] and the absorption of the intermediate products on the photocatalyst surface to cover the active sites[55].

Fig. 4d shows the concentration of CH_4 evolution when the reference experiments were carried out. When the experiment was carried out in the absence of H_2O, catalyst or light irradiation, very little CH_4 was detected. Since there is about 1 ppm of CH_4 in the natural air, the CH_4 in the above-mentioned experiments is

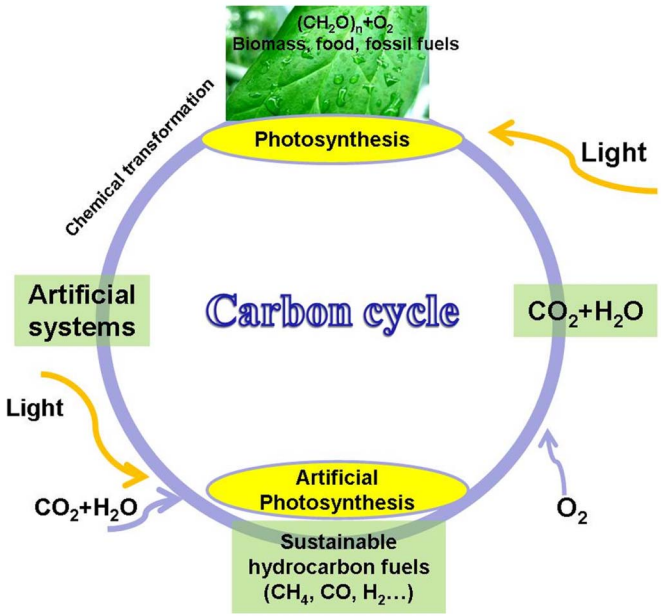

Figure 5 | Schematic illustration of the potential realization of global carbon neutral cycle of this process.

considered as the contamination from air during samplings. Nevertheless, in the case that the CO_2 gas was replaced by Ar gas, a small amount of CH_4 was found which should be generated from the photoreduction of the remaining CO_2 on the sample surface[56]. Consequently, all the above-mentioned reference experiments prove that the H_2O supplies protons, CO_2 offers a carbon source, and the photocatalyst gives the redox potentials for the whole reaction to finally produce CO and CH_4.

Discussion

We demonstrated a design strategy for a promising 3D APS architecture as an efficient mass flow network for improved gas diffusion and light harvesting relying on the morphological replacement of leaf's 3D hierarchical architecture into perovskite titanates. We believe that a general method for the construction of 3D APS architectures of $ATiO_3$ (A = Sr, Ca, and Pb) achieved here through the conversion of the morphological elements of NPS into APS, can be extended to other multi-metallic oxides, such as tantalates (*e.g.* $NaTaO_3$, $KTaO_3$, $Sr_2Ta_2O_7$), niobates (*e.g.* $NaNbO_3$) via modified sol-gel or polymerizable complex method. Such methodology can also be extended to polymeric metal-free photocatalysts, such as graphitic carbon nitride (g-C_3N_4) based on earth-abundant elements. To the best of our knowledge this is the first example utilizing biological systems as an "architecture-directing agent" for the synthesis of APS for CO_2 photoreduction. Assisted by the large variety of green plants and biological systems[33], this design strategy hints at a more general principle for the design of APS architectures with a great variety of useful and optimized geometries. Indeed, hierarchical constructions on a scale ranging from nanometers to millimeters are characteristic of biological structures and introduce the capacity to answer physical or chemical demands occurring at these different levels. Many of these hierarchical, elaborate structures are barely attainable by man-made materials. This strategy could be extended to various hierarchical biological systems (*e.g.* photosynthetic diatoms, radiolarians, etc.). By using biomass as the raw resources, this strategy also has great significance for the realization of global carbon neutral cycle as well as for the ultimate goal of solar energy utilization in tailor-made synthesis of fine chemicals and solar fuel from CO_2 (Fig. 5). An area for further study is the computation, simulation and modeling of leaf's 3D concept prototypes, and biomimetic synthesis of the complicated networks (e.g. with the assistance of 3D inkjet printing technology) for large scale production. Finally, this study opens possibilities of applications of leaf's 3D architecture prototype or other architecture models in nature for the field of artificial photosynthesis as well as many other energy capture, conversion and storage areas, such as solar cells, fuel cells, battery electrodes, and so forth.

Methods

Synthesis of APS of $ATiO_3$ (A = Sr, Ca, Pb). Fresh green leaves (Cherry Blossom) were cut into 2 cm × 2 cm pieces and washed with deionized water, then they were immersed in 5% diluted HCl overnight to get rid of Mg, K, Ca, P, S and other ions. Afterwards, the treated leaves were washed with deionized water and ethanol several times. A typical preparation for APS_{SrTiO3} is as follows: Titanium tetrabutoxide (10 mmol) was dissolved and stirred in heated (70°C) acetylacetone while $Sr(Ac)_2$•$0.5H_2O$ (10 mmol) was dissolved and stirred in heated (70°C) ethanol/CH_3COOH (v : v = 1 : 1) solution. Then the two solutions were mixed, and then P123 (4 g) was added with stirring at 70°C for 4 h. The pretreated leaves were immersed in the precursors for eight hours at room temperature and then washed with ethanol for four times. The infiltrated leaves were dried at 100°C for one day and then calcined at 600°C for 10 h in O_2 atmosphere at a heating rate of 1°C min^{-1} for multi-metal oxides crystallization and for organics removal. For the synthesis of $CaTiO_3$ and $PbTiO_3$, $Ca(Ac)_2$•H_2O and $Pb(Ac)_2$•$3H_2O$ were used instead of $Sr(Ac)_2$•$0.5H_2O$, respectively. For the synthesis of $CaTiO_3$, $Ca(Ac)_2$•H_2O was dissolved and stirred in heated (70°C) CH_3COOH solution instead of ethanol/CH_3COOH solution. The powder constituents of APS were obtained by grounding the APS with a mortar. The referenced ATO were synthesized without using leaves as templates.

Loading the co-catalysts. The loading of Pt, Au, Ag, Cu were performed by a photodeposition method using H_2PtCl_6•$6H_2O$, $HAuCl_4$•$3H_2O$, $AgNO_3$, $Cu(NO_3)_2$ as the Pt, Au, Ag, and Cu sources, respectively. Typically, 0.2 g photocatalyst, 220 ml distilled water, 50 ml methanol and a given amount of noble metal sources (1 wt%) were placed in a glass vessel. The reaction solution was irradiated by a 300 W Xe arc lamp for 1h with stirring. Then, the photocatalysts were filtered, washed thoroughly with deionized water, dried in a vacuum at room temperature for 4 h and then dried in an oven at 100°C for 10 h. The loading of Au was also performed by a precipitation method for comparison. The precipitation procedure was done at 343 K and pH 9 for 4 h with 1 wt% $HAuCl_4$•$3H_2O$ as the Au source, using (0.2 M) NaOH to maintain the pH constant. The catalyst was then recovered, filtered, washed with deionized water, and dried at 373 K overnight. Finally, the powder was calcined at 473 K in air for 4 h[51].

The loading of RuO_2: The loading of RuO_2 was performed by impregnating photocatalyst powders with the solution of ruthenium complex, $Ru_3(CO)_{12}$ (Aldrich Chemical Co., 99% pure) in tetrahydrofuran (THF). The impregnated samples were stirred at 60°C for 4h, dried at 60°C, and oxidized at 350°C in air for 2 h to convert ruthenium complex species to ruthenium oxide.

The loading of NiOx: The $SrTiO_3$ particles were added to 20 mL of an aqueous $Ni(NO_3)_2$•$6H_2O$ solution (1 wt% loading of NiO: STO) and thoroughly mixed in a sonication bath for 10 min. This solution was dried at 100°C and then calcined for 1h at 350°C in air. The air above the solid was flushed with N_2 and then replaced by H_2, and the sample was heated to 500°C for 2 h to reduce nickel. The final product was obtained after another 1h of heating at 200°C in an O_2 atmosphere.

CO_2 photoreduction measurements. The CO_2 photoreduction experiments were carried out in a gas closed circulation system with an upside window (Figure S13). The catalyst (50 mg) was dispersed on a small glass cell and then located in a Pyrex reaction cell. After that, 2 mL of distilled water was added into the gas closed reaction system. The whole system was then evacuated and filled with 80 kPa of pure CO_2 gas. The light source was a 300 W Xe arc lamp (ILC Technology, CERMAX LX-300). An L-42 (Hoya Corp., Japan) cutoff filter was used to obtain visible light ($\lambda > 420$ nm). The organic products were sampled and measured with a gas chromatograph (GC-14B, Shimadzu) equipped with a flame ionization detector (FID) according to the standard curves. The H_2 and O_2 evolution was measured with an online gas chromatograph (GC-8A, Shimadzu) with a TCD detector according to the standard curve.

Characterization. The crystal structure of samples was determined with an X-ray diffractometer (Rint-2000, Rigaku Co., Japan) with Cu Kα radiation. The diffuse reflection spectra were measured with an integrating sphere equipped UV−visible recording spectrophotometer (UV-2500PC, Shimadzu Co., Japan) using $BaSO_4$ as a reference, and the optical absorptions were converted from the reflection spectra according to the Kubelka−Munk equation. Scanning Electron Microscopy (SEM) images were recorded to observe the morphology with scanning electron microscope (JEOL 6700F field emission scanning electron microscope). Transmission electron microscopy images and high-resolution images were recorded with a field emission transmission electron microscope (2100F, JEOL Co., Japan) operated at 200 kV. The specific surface areas were determined with a surface-area analyzer (BEL Sorp-II mini, BEL Japan Co., Japan) by the Brunauer−Emmett−Teller (BET) method. Mercury porosimetry measurements were performed using an Autopore IV 9500 (Micromertitics Company).

1. Listorti, A., Durrant, J. & Barber, J. Artificial Photosynthesis: solar to fuel. *Nat. Mater.* **8**, 929–930 (2009).
2. Lewis, N. S. & Nocera, D. G. Powering the planet: Chemical challenges in solar energy utilization. *Proc. Natl. Acad. Sci. USA* **103**, 15729–15735 (2006).
3. Tachibana, Y., Vayssieres, L. & Durrant, J. R. Artificial photosynthesis for solar water-splitting. *Nat. Photonics* **6**, 511–518 (2012).
4. Antonietti, M. On the way to artificial photosynthesis: simple materials and system designs for photoelectrodes. *Angew. Chem. Int. Ed.* **52**, 1086–1087 (2013).
5. Kalyanasundaram, K. & Graetzel, M. Artificial Photosynthesis: biomimetic approaches to solar energy conversion and strorage. *Current opinion in Biotechnology* **21**, 298–310 (2010).
6. Michl, J. Photochemical CO_2 reduction: towards an artificial leaf? *Nat. Chem.* **3**, 268–269 (2011).
7. Bensaid, S., Centi, G., Garrone, E., Perathoner, S. & Saracco, G. Towards artificial leaves for solar hydrogen and fuels from carbon dioxide. *ChemSusChem* **5**, 500–521 (2012).
8. Halmann, M. Photoelectrochemical reduction of aqueous carbon oxides on p-type gallium phosphide in liquid junction solar cells. *Nature* **275**, 115–116 (1978).
9. Inoue, I., Fujishima, A., Konishi, S. & Honda, K. Photoelectrocatalytic reduction of carbon dioxide in aqueous suspensions of semiconductor powders. *Nature* **277**, 637–638 (1979).
10. Roy, S. C., Varghese, O. K., Paulose, M. & Grimes, G. A. Toward solar fuels: photocatalytic conversion of carbon dioxide to hydrocarbons. *ACS Nano* **4**, 1259–1278 (2010).
11. Hoffmann, M. R., Moss, J. A. & Baum, M. M. Artificial photosynthesis: semiconductor photocatalytic fixation of CO_2 to afford higher organic compounds. *Dalton Trans.* **40**, 5151 (2011).
12. Mori, K., Yamashita, H. & Anpo, M. Photocatalytic reduction of CO_2 with H_2O on various titanium oxide photocatalysts. *RSC Advances* **2**, 3165–3172 (2012).
13. Dhakshinamoorthy, A., Navalon, S., Corma, A. & Garcia, H. Photocatalytic CO_2 reduction by TiO_2 and related titanium containing solids. *Energy Environ. Sci.* **5**, 9217 (2012).
14. Liu, Q., Zhou, Y., Kou, J., Chen, X., Tian, Z., Gao, J., Yan, S. & Zou, Z. G. High-yield synthesis of ultralong and ultrathin Zn_2GeO_4 nanoribbons toward improved photocatalytic reduction of CO_2 into renewable hydrocarbon fuel. *J. Am. Chem. Soc.* **132**, 14385–14387 (2010).
15. Zhang, N., Ouyang, S. X., Li, P., Zhang, Y. J., Xi, G. C., Kako, T. & Ye, J. H. Ion-exchange synthesis of a micro/mesoporous Zn_2GeO_4 photocatalysts at room temperature for photoreduction of CO_2. *Chem. Commun.* **47**, 2041–2043 (2011).
16. Zhang, N., Ouyang, S. X., Kako, T. & Ye, J. H. Mesoporous zinc germanium oxynitride for CO_2 photoreduction under visible light. *Chem. Commun.* **48**, 1269–1271 (2012).
17. Yan, S. C., Ouyang, S. X., Gao, J., Yang, M., Feng, J. Y., Fan, X. X., Wan, L. J., Li, Z. S., Ye, J. H., Zhou, Y. & Zou, Z. G. A room-temperature reactive-template route to mesoporous $ZnGa_2O_4$ with improved photocatalytic activity in reduction of CO_2. *Angew. Chem. Int. Ed.* **49**, 6400–6404 (2010).
18. Matsumoto, Y., Obata, M. & Hombo, J. Photocatalytic reduction of carbon dioxide on p-type $CaFe_2O_4$ powder. *J. Phys. Chem.* **98**, 2950–2951 (1994).
19. Iizuka, K., Wato, T., Miseki, Y., Saito, K. & Kudo, A. Photocatalytic reduction of carbon dioxide over Ag cocatalyst-loaded $ALa_4Ti_4O_{15}$ (A = Ca, Sr, and Ba) using water as a reducing reagent. *J. Am. Chem. Soc.* **133**, 20863–20868 (2011).
20. Xi, G. C., Ouyang, S. X., Li, P., Ye, J. H., Ma, Q., Su, N., Bai, H. & Wang, C. Ultrathin $W_{18}O_{49}$ nanowires with diameters below 1nm: synthesis, near-infrared absorption, photoluminescence, and photochemical reduction of carbon dioxide. *Angew. Chem. Int. Ed.* **51**, 2395–2399 (2012).
21. Takahashi, R., Sato, S., Sodesawa, T., Arai, K. & Yabuki, M. Effect of diffusion in catalytic dehydration of alcohol over silica-alumina with continuous macropores. *J. Catal.* **229**, 24–29 (2005).
22. Mitchell, S., Michels, N. L., Kunze, K. & Ramirez, J. P. Visualization of hierarchically structured zeolites bodies from macro to nano length scales. *Nat. Chem.* **4**, 825–831 (2012).
23. Li, Y., Fu, Z. Y. & Su, B. L. Hierarchically structured porous materials for energy conversion and storage. *Adv. Funct. Mater.* **22**, 4634–4667 (2012).
24. Sanchez, C., Arribart, H. & Guille, M. M. G. Biomimetism and bioinspiration as tools for the design of innovative materials and systems. *Nat. Mater.* **4**, 277–288 (2005).
25. Barber, J. Biological solar energy. *Philos. Trans. R. Soc. Lond. Ser. A* **365**, 1007–1023 (2007).
26. Parkhurst, D. F. Diffusion of CO_2 and other gases inside leaves. *New Phytol.* **126**, 449–479 (1994).
27. Brodribb, T. J., Feild, T. S. & Sack, L. Viewing leaf structure and evolution from a hydraulic perspective. *Functional Plant Biology* **37**, 488–498 (2010).
28. Niinemets, U. & Sack, L. Structural determinants of leaf light harvesting capacity and photosynthetic potentials. *Prog. Bot.* **67**, 385–419 (2006).
29. Shimoni, E., Rav-Hon, O., Ohad, I., Brumfeld, V. & Reich, Z. Three-dimensional organization of higher-plant chloroplasts thylakoid membranes revealed by electron tomography. *Plant Cell* **17**, 2580–2586 (2005).
30. Cowan, I. R. Economics of carbon fixation in higher plants. In: *On the economy of plant form and function*. (ed. Givnish, T. J.). 133–170 (Cambridge University Press, 1986).
31. Niklas, K. J. A mechanical perspective on foliage leaf form and function. *New Phytologist* **143**, 19–31 (1999).
32. Zwieniecki, M. A., Brodribb, T. J. & Holbrook, N. M. Hydraulic design of leaves: insights from rehydration kinetics. *Plant Cell and Environment* **30**, 910–921 (2007).
33. Fan, T. X., Chow, S.-K. & Zhang, D. Biomorphic mineralization: from biology to materials. *Progress in Materials Science* **54**, 542–659 (2009).
34. Schnepp, Z. Biopolymers as a flexible resource for nanochemistry. *Angew. Chem. Int. Ed.* **52**, 1096–1108 (2013).
35. Sotiropoulou, S., Yajaira, S.-S., Mark, S. S. & Batt, C. A. Biotemplated nanostructured materials. *Chem. Mater.* **20**, 821–834 (2008).
36. Zhou, H., Li, X. F., Fan, T. X., Osterloh, F. E., Ding, J., Sabio, E. M., Zhang, D. & Guo, Q. X. Artificial inorganic leafs for efficient photochemical hydrogen production inspired by natural photosynthesis. *Adv. Mater.* **22**, 951–956 (2010).
37. Tong, H., Ouyang, S. X., Bi, Y. P., Umezawa, N., Oshikiri, M. & Ye, J. H. Nano-photocatalytic materials: possibilities and challenges. *Adv. Mater.* **24**, 229–251 (2012).
38. Chen, X., Shen, S., Guo, L. & Mao, S. S. Semiconductor-based photocatalytic hydrogen generation. *Chem. Rev.* **110**, 6503–6570 (2010).
39. Osterloh, F. E. Inorganic materials as catalysts for photochemical splitting of water. *Chem. Mater.* **20**, 35–54 (2008).
40. Chen, X., Li, C., Gratzel, M., Kostecki, R. & Mao, S. S. Nanomaterials for renewable energy production and storage. *Chem. Soc. Rev.* **41**, 7909–7937 (2012).
41. Wrighton, M. S., Ellis, A. B., Wolczanski, P. T., Morse, D. L., Abrahamson, H. B. & Ginley, D. S. Strontium titanate photoelectrodes: efficient photoassisted electrolysis of water at zero applied potential. *J. Am. Chem. Soc.* **98**, 2774–2779 (1976).
42. Halasi, G., Schubert, G. & Solymosi, F. Photodecomposition of formic acid on N-doped and metal-promoted TiO_2 production of CO-free H_2. *J. Phys. Chem. C* **116**, 15396–15405 (2012).
43. Chiarello, G. L., Aguirre, M. H. & Selli, E. Hydrogen production by photocatalytic steam reforming of methanol on noble metal-modified TiO_2. *J. Catal.* **273**, 182–190 (2010).
44. Cindrella, L., Kannan, A. M., Lin, J. F., Saminathan, K., Ho, Y., Lin, C. W. & Wertz, J. Gas diffusion layer for proton exchange membrane fuel cells-a review. *J. Power Sources* **194**, 146–160 (2009).
45. Ishitani, O., Inoue, C., Suzuki, Y. & Ibusuki, T. Photocatalytic reduction of carbon dioxide to methane and acetic acid by an aqueous suspension of metal-deposited TiO_2. *J. Photochem. Photobiol. A* **72**, 269–271 (1993).
46. Gorem, Z., Willner, I., Nelson, A. J. & Frank, A. J. Selective photoreduction of carbon dioxide/bicarbonate to formate by aqueous suspensions and colloids of palladium-titania. *J. Phys. Chem.* **94**, 3784–3790 (1990).
47. Ouyang, S., Tong, H., Umezawa, N., Cao, J., Li, P., Bi, Y., Zhang, Y. & Ye, J. Surface alkalinization induced enhancement of photocatalytic H_2 evolution over $SrTiO_3$-based photocatalysts. *J. Am. Chem. Soc.* **134**, 1974–1977 (2012).
48. Shimura, K., Kato, S., Yoshida, T., Itoh, H., Hattori, T. & Yoshida, H. Photocatalytic steam reforming of methane over sodium tantalite. *J. Phys. Chem. C* **114**, 3493–3503 (2010).
49. Hinogami, R., Nakamura, Y., Yae, S. & Nakato, Y. Modification of semiconductor surface with ultrafine metal particles for efficient photoelectrochemical reduction of carbon dioxide. *Appl. Surf. Sci.* **121/122**, 301–304 (1997).
50. Chen, Y., Li, C. W. & Kanan, M. W. Aqueous CO_2 reduction at very low overpotential on oxide-derived Au nanoparticles. *J. Am. Chem. Soc.* **134**, 19969–19972 (2012).
51. Silva, C. G., Juarez, R., Marino, T., Molinari, R. & Garcia, H. Influence of excitation wavelength (UV or visible light) on the photocatalytic activity of titania containing gold nanoparticles for the generation of hydrogen or oxygen from water. *J. Am. Chem. Soc.* **133**, 595–602 (2011).
52. Lira, E., Wendt, S., Huo, P., Hansen, J., Streber, R., Porsgaard, S., Wei, Y., Bechstein, R., Lagsgaard, E. & Besenbacher, F. The importance of bulk Ti^{3+} defects in the oxygen chemistry on titania surfaces. *J. Am. Chem. Soc.* **133**, 6529–6532 (2011).
53. Yuliati, L., Hattori, T., Itoh, H. & Yoshida, H. Photocatalytic nonoxidative coupling of methane on gallium oxide and silica-supported gallium oxide. *J. Catal.* **257**, 396–402 (2008).
54. Kedzierzawski, P. & Augustynski, J. Poisoning and activation of the gold cathode during electroreduction of CO_2. *J. Electrochem. Soc.* **141**, L58–60 (1994).
55. Liu, Q., Zhou, Y., Tian, Z., Chen, X., Cao, J. & Zou, Z. Zn_2GeO_4 crystal splitting toward sheaf-like, hyperbranched nanostructures and photocatalytic reduction of CO_2 into CH_4 under visible light after nitridation. *J. Mater. Chem.* **22**, 2033–2038 (2012).
56. Dimitrijevic, N. M., Vijayan, B. K., Poluektov, O. G., Rajh, T., Gray, K. A., He, H. & Zapol, P. Role of water and carbonates in photocatalytic transformation of CO_2 to CH_4 on titania. *J. Am. Chem. Soc.* **133**, 3964–3971 (2011).

Acknowledgments

We are grateful for financial support by the World Premier International Research Center Initiative on Materials Nanoarchitectonics, MEXT, Japan and the National Natural Science Foundation of China (51102163).

Author contributions

H. Zhou designed the experiment, synthesized the materials and performed the measurements. J. Ye supervised the project. J. Guo and P. Li assisted with the photocatalytic performances measurement. H. Zhou wrote the paper. J. Ye, T. Fan and D. Zhang commented on the manuscript writing and the results discussion. All the authors discussed the results and comments on the manuscript.

Additional information

Supplementary information accompanies this paper at http://www.nature.com/scientificreports

Competing financial interests: The authors declare no competing financial interests.

License: This work is licensed under a Creative Commons Attribution-NonCommercial-NoDerivs 3.0 Unported License. To view a copy of this license, visit http://creativecommons.org/licenses/by-nc-nd/3.0/

How to cite this article: Zhou, H. *et al*. Leaf-architectured 3D Hierarchical Artificial Photosynthetic System of Perovskite Titanates Towards CO_2 Photoreduction Into Hydrocarbon Fuels. *Sci. Rep.* **3**, 1667; DOI:10.1038/srep01667 (2013).